Astroparticle Physics 2023/24

1. Historical introduction - basic properties of cosmic rays
2. Hadronic interactions and accelerator data
3. Cascade equations
4. Electromagnetic cascades
5. Extensive air showers
6. Detectors for extensive air showers
7. High-energy cosmic rays and the knee in the energy spectrum of cosmic rays
8. Radio detection of extensive air showers
9. Acceleration, Astrophysical accelerators and beam dumps
10. Extragalactic propagation of cosmic rays
11. Ultra-high-energy energy cosmic rays
12. Astrophysical gamma rays and neutrinos
13. Neutrino astronomy
14. Gamma-ray astronomy

lecture 2
Hadronic interactions and accelerator data

Gaisser chapter 4

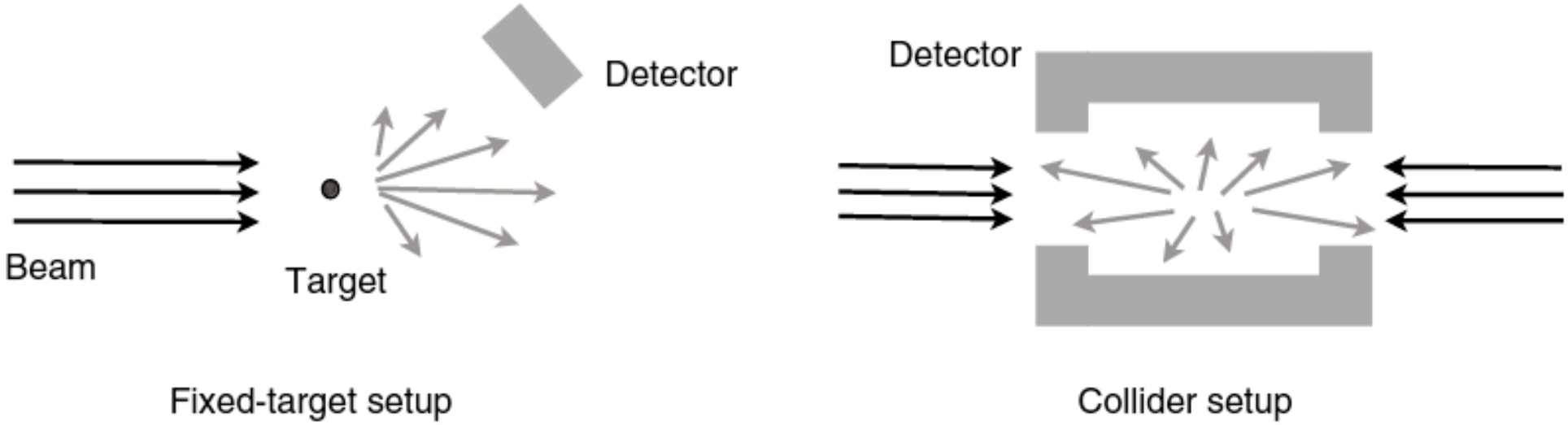

Figure 4.1 Fixed-target and collider setups for measuring particle production at accelerators. The particle detectors are indicated in gray and might provide tracking (of charged particles) and calorimetry. The energies of the two beams of collider experiments are typically the same except if different particles are accelerated such as electrons and protons or protons and nuclei.

$$E_{\mathrm{cm}} = E_a^\star + E_b^\star.$$ **center of mass energy**

$$s = (p_a^\star + p_b^\star)^2 = (p_a + p_b)^2 = E_{\mathrm{cm}}^2.$$ **Mandelstam variable (Lorentz invariant)**

$$E_{\mathrm{cm}} = \sqrt{s} = \left(2E_a m_b + m_a^2 + m_b^2\right)^{1/2} \approx \sqrt{2E_a m_b}.$$ **energy in fixed traget exp. only proportional sqrt(s)**

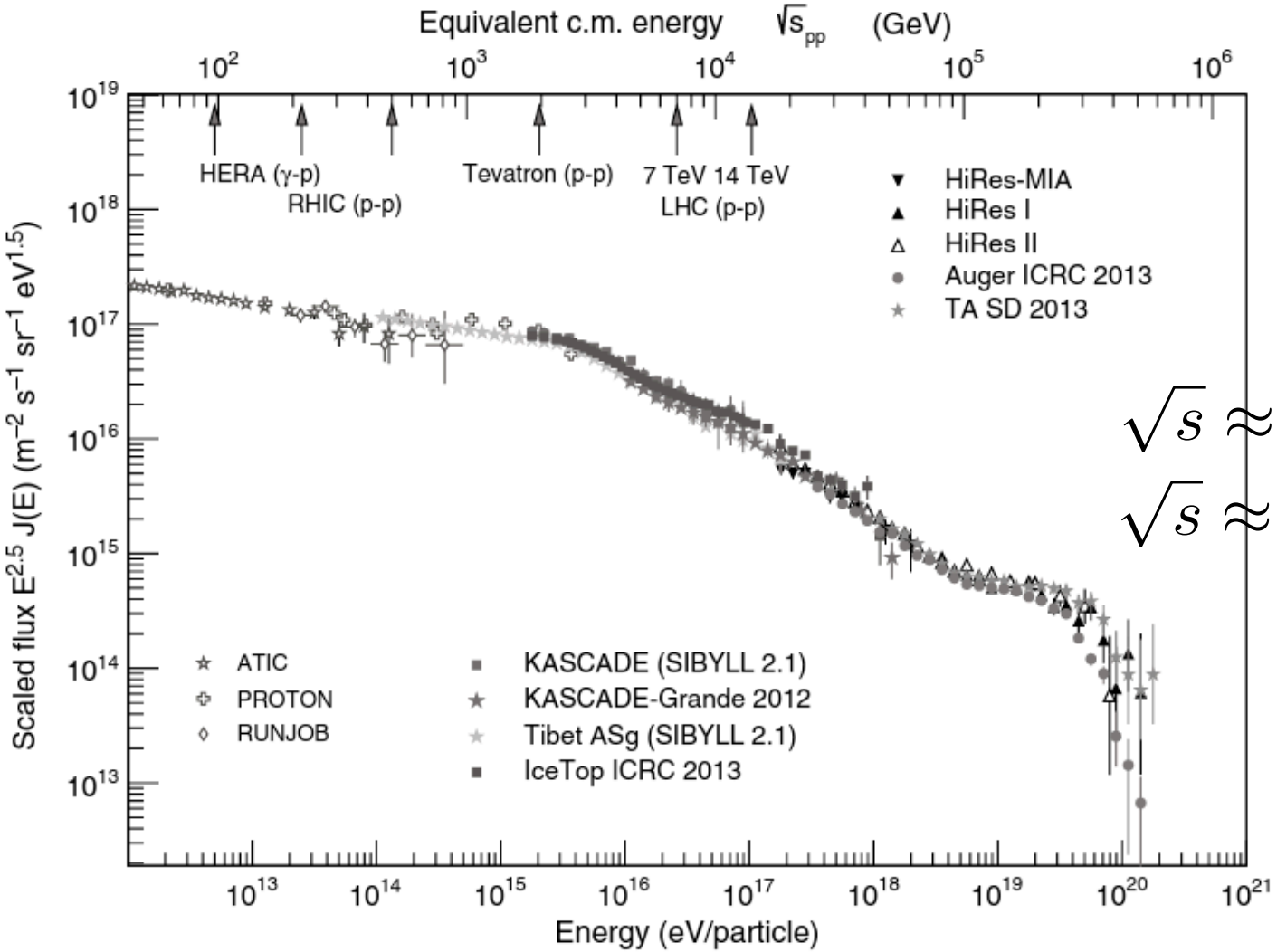

$\sqrt{s} \approx 430$ TeV **p**

$\sqrt{s} \approx 57$ TeV **Fe**

Figure 4.2 All-particle flux of cosmic rays scaled by $E^{2.5}$ (from [33], updated). The x axis at the top shows the equivalent nucleon–nucleon c.m. energy of the interaction of protons of the cosmic ray flux with a nucleon of the air. The energies reached by different colliders are marked by arrows. Fixed target experiments have maximum beam energies of, for example, 350 GeV (NA49, NA61 at CERN) and 800 GeV (SELEX at Tevatron), which is below the lowest energy shown here. The LHC collider was the first accelerator that allowed the study of interactions at energies above the knee in the cosmic ray spectrum.

Cross section

1b = 10^{-24} cm^2

$$\sigma_j = \frac{1}{\Phi_a}\frac{\mathrm{d}N_j}{\mathrm{d}t}.$$ cross section for process *j*

$$, \Phi_a = \mathrm{d}N_a/(\mathrm{d}A\,\mathrm{d}t).$$ flux of particles crossing area *dA*

secondary particle production: inclusive cross section

$$\frac{\mathrm{d}\sigma_{ab\to c}}{\mathrm{d}^3 p_c} = \frac{1}{\Phi_a}\frac{\mathrm{d}N_c}{\mathrm{d}^3 p_c\,\mathrm{d}t},$$

multiplicity of particles

$$n_c = \frac{\sigma_{ab\to c}}{\sigma_{\mathrm{ine}}} = \frac{\mathrm{d}N_{ab\to c}/\mathrm{d}t}{\mathrm{d}N_{\mathrm{ine}}/\mathrm{d}t}.$$

Inclusive cross sections can be measured straight forward but do not contain correlations between different particles produced.
Exclusive cross sections contain the full information of the final state.

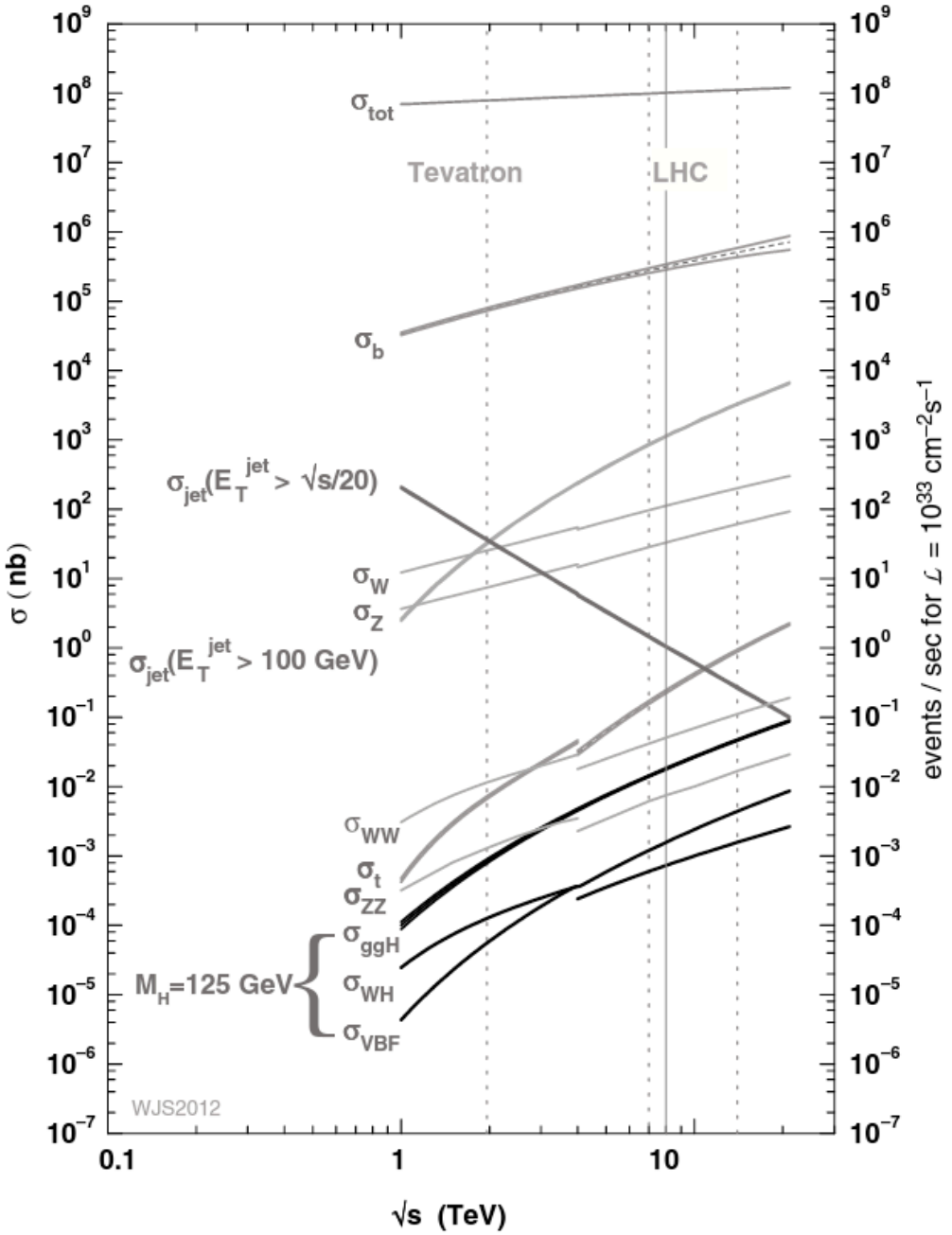

Figure 4.3 Comparison of cross sections measured at hadron colliders, from [121]. Shown are the total p-p cross section and inclusive production cross sections for jets and a number of different particles. The cross sections have been calculated for p-$\bar{p}$ interactions (Tevatron) up to $\sqrt{s} = 3.5\,\text{TeV}$ and for p-p interactions (LHC) above this energy, leading to a small discontinuity for processes depending on the valence quark flavors.

Final state kinematics and phase space coverage

The general structure of the phase space distribution of final state particles produced in high-energy interactions can be derived from the parton model of hadrons and the fact that small momentum transfers dominate the interactions between partons in QCD. For example, we consider the interaction of protons at a collider; see Figure 4.4. Due to confinement, the partons are bound in hadrons prior to the collision. The Heisenberg uncertainty relation implies $\Delta p\, \Delta x \sim 1$ and allows us to estimate the typical parton momenta

$$\Delta p_\perp \sim \frac{1}{R} \sim 200\,\text{MeV}, \qquad \Delta p_\parallel \sim \frac{1}{R'} = \left(\frac{E_p}{m_p}\right)\frac{1}{R} \sim \frac{1}{5}E_p. \quad (4.10)$$

If the momentum transfer of the interaction is small, the final state particles will resemble the kinematic distribution of the initial partons. Thus, while having typically only small transverse momenta, the secondary particles are expected to populate a large fraction of the longitudinal phase space.

Final state kinematics and phase space coverage

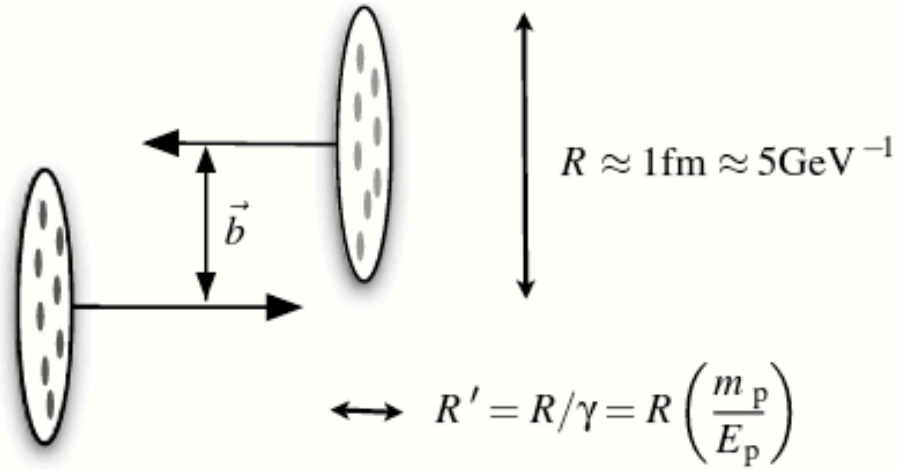

Figure 4.4 Illustration of the effect of Lorentz contraction on the longitudinal and transverse dimensions of colliding particles as seen from the lab system. The Lorentz factor of the beam particles, here assumed to be protons, is $\gamma = E_p/m_p$. The transverse displacement of the particle trajectories is given by the impact parameter $\vec{b}$.

In first approximation the longitudinal and transverse degrees of freedom factorize. The longitudinal momentum is conveniently measured relative to the maximum momentum a particle can have. In contrast, transverse momenta are not re-scaled. This is reflected in the set of variables given in Table 4.1 that are commonly used for describing the momentum of final state particles.

Table 4.1 *Kinematic variables for describing secondary particles*

Variable	Definition	Comment
$x_F \equiv x^\star$	$\frac{p_\parallel^\star}{p_{\parallel,\max}^\star} \approx \frac{2p_\parallel^\star}{\sqrt{s}}$	Feynman x
x_R	$\frac{E^\star}{E_{\max}^\star} \approx 2\frac{E^\star}{\sqrt{s}}$	radial x
m_T	$\sqrt{p_\perp^2 + m^2}$	transverse mass
$x_{\text{lab}} \equiv x_L$	$E_{\text{lab}}/E_{\text{lab,max}}$	$\approx E_{\text{lab}}/E_{\text{beam}}$
y	$\frac{1}{2}\ln\frac{E+p_\parallel}{E-p_\parallel}$	rapidity
η	$-\ln\tan(\theta/2)$	pseudorapidity

Often the mass of a secondary particle cannot be measured. Then the *pseudorapidity* η is used as an approximation of the rapidity – the higher the momentum of the particle relative to its mass, the better the approximation,

$$\eta = \frac{1}{2} \ln \frac{|p| + p_\parallel}{|p| - p_\parallel} = -\ln \tan \frac{\theta}{2}. \tag{4.14}$$

Here θ is the polar angle of the particle with respect to the beam axis. Pseudorapidity and rapidity of massless particles are identical.

Particle detectors employed in high-energy physics cover only a part of the phase space of final state particles. In particular it is very difficult to measure secondary particles close to any beam direction, and only charged particles above a detector specific momentum threshold of typically $100 - 250\,\mathrm{MeV}$ can be detected reliably. Charged particle tracking is typically achieved in an angular range equivalent to $|\eta| \lesssim 3$. A comparison of expected particle distributions and examples of typical phase space coverages are shown in Figure 4.5. The detectors allow the measurement of the bulk of the secondary particles. For cosmic ray applications, however, the energy flow is a better measure of the importance of the different phase space regions. Many high-energy secondaries are produced with very small angles to the beam pipe and cannot be detected.

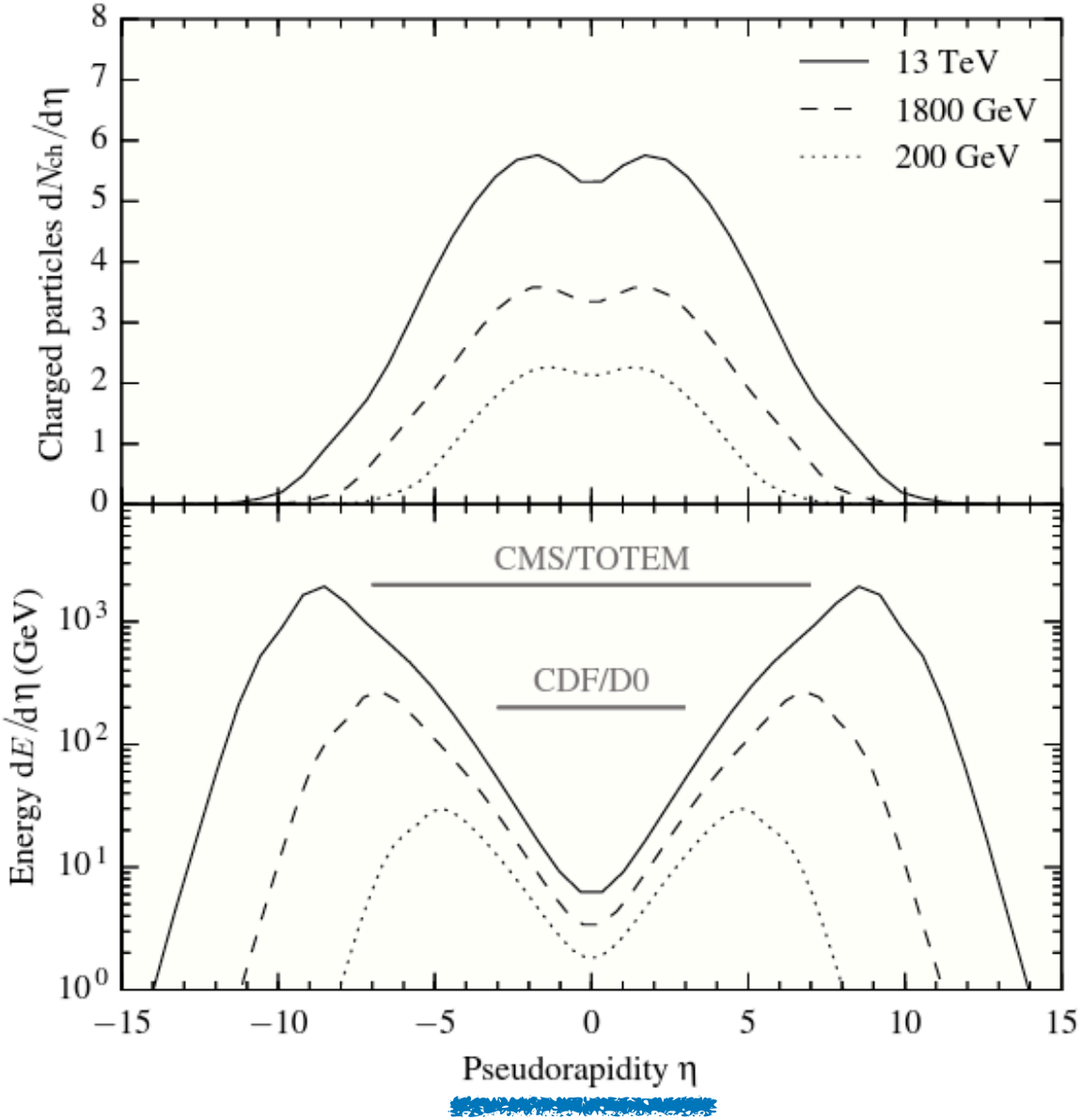

Figure 4.5 Phase space coverage of multi-purpose detectors at high-energy colliders. Shown are the charged particle multiplicity and the total energy of the final state particles as function of pseudorapidity for different c.m. energies. The coverage in pseudorapidity of the CMS detector extended by TOTEM for forward tracking is shown as an example for LHC ($\sqrt{s} = 13\,\text{TeV}$) and that of the CDF and D0 detectors for the Tevatron collider ($\sqrt{s} = 1.8\,\text{TeV}$).

CALIBRATION OF HADRON INTERACTION MODELS AT LHC

p-p 450 GeV + 450 GeV → $E_{lab} \sim 4 \cdot 10^{14}$ eV
p-p 3.5 TeV + 3.5 TeV → $E_{lab} \sim 3 \cdot 10^{16}$ eV
p-p 6.5 TeV + 6.5 TeV → $E_{lab} \sim 9 \cdot 10^{16}$ eV

- Total cross section ↔ TOTEM, ATLAS, CMS
- Multiplicity ↔ Central detectors
- Inelasticity/Secondary spectra ↔ Forward calorimeters (**LHCf**, ZDCs)

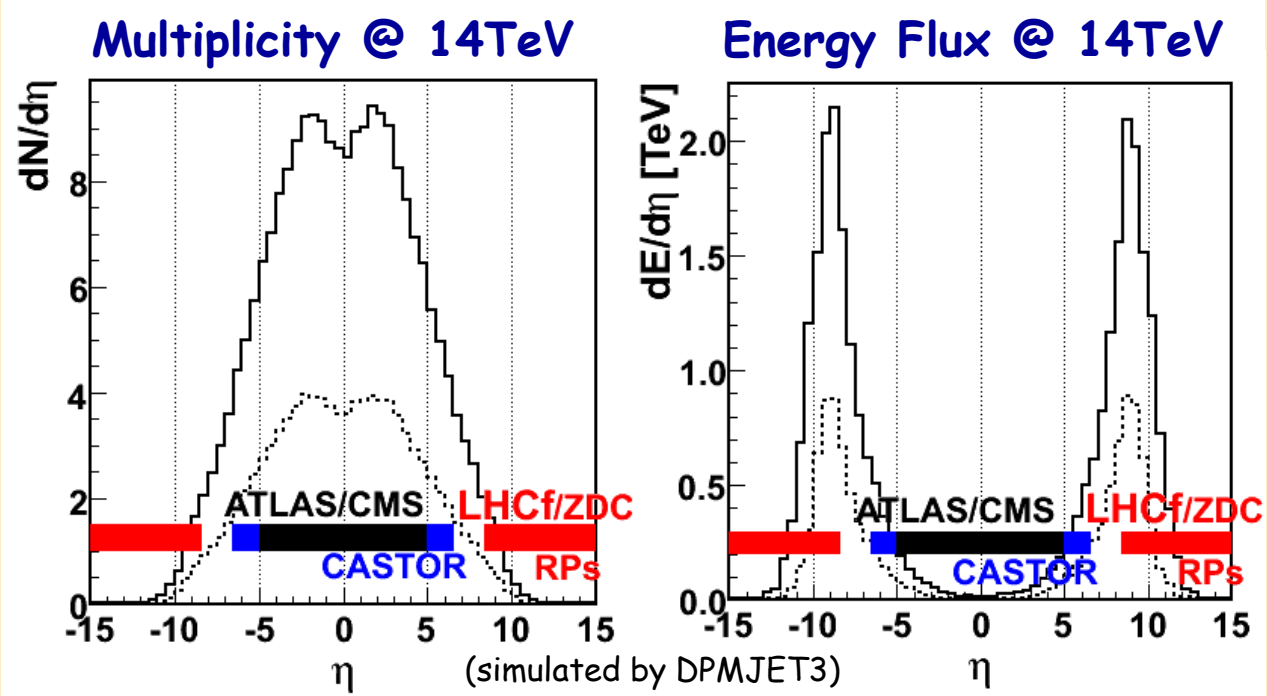

LHCf EXPERIMENTAL SET-UP

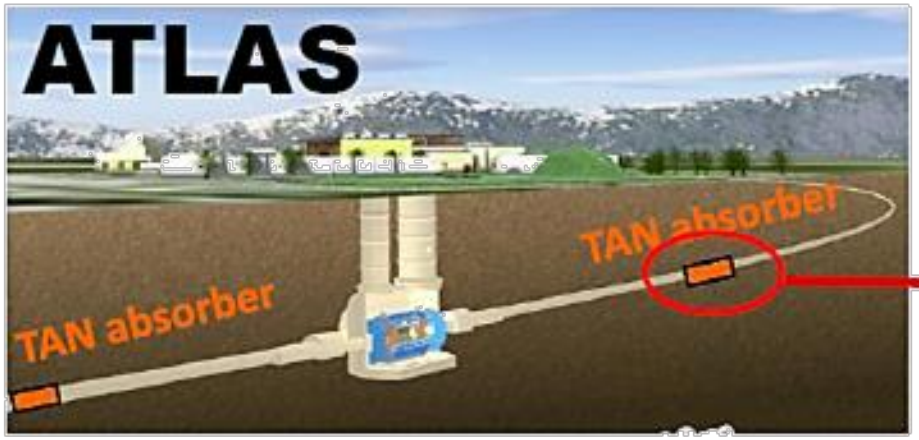

Detectors are located inside the TAN absorber for neutral particles

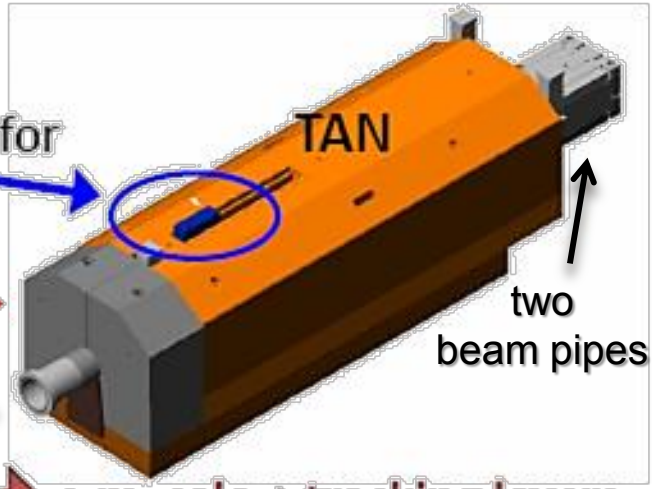

The LHCf detectors measure energy and impact point of γ and n → e.m. calo + tracking layers

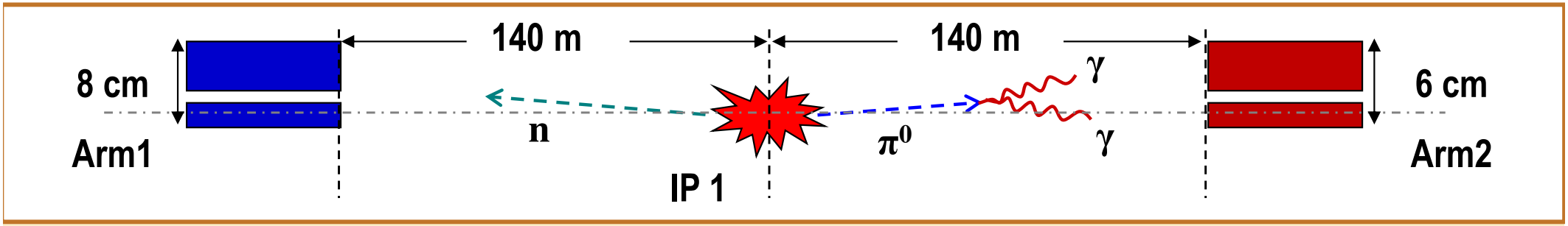

Two independent detectors on both sides of IP1

- ✓ Redundancy
- ✓ Background rejection (esp. beam-gas)

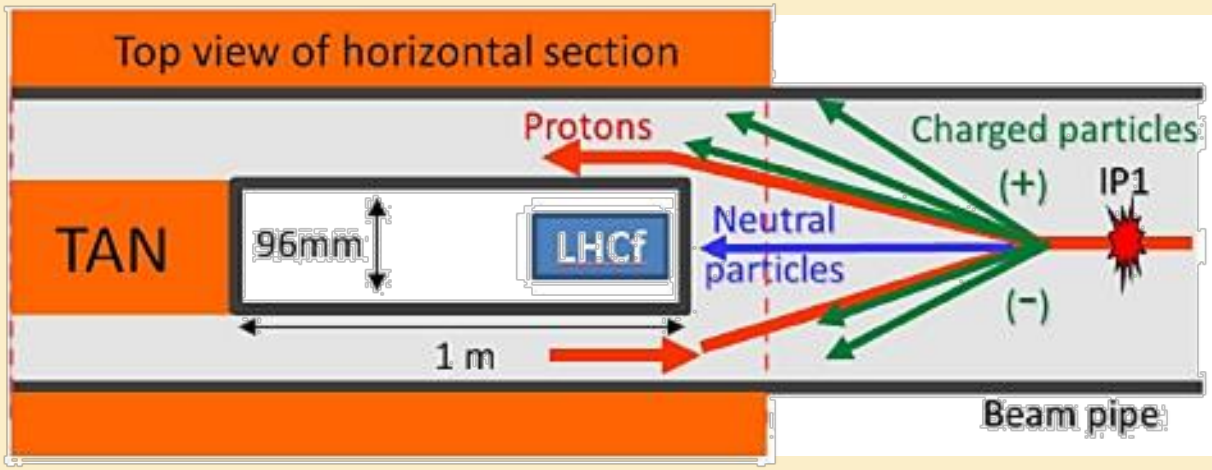

Total and elastic cross sections

It is still not possible to calculate total and elastic cross sections of hadrons within QCD. Measurements at accelerators have to be combined with phenomenological models to obtain a description of cross sections over the energy range of importance for cosmic ray physics. In addition, at the highest energies, measurements of air showers provide constraints on cross sections.

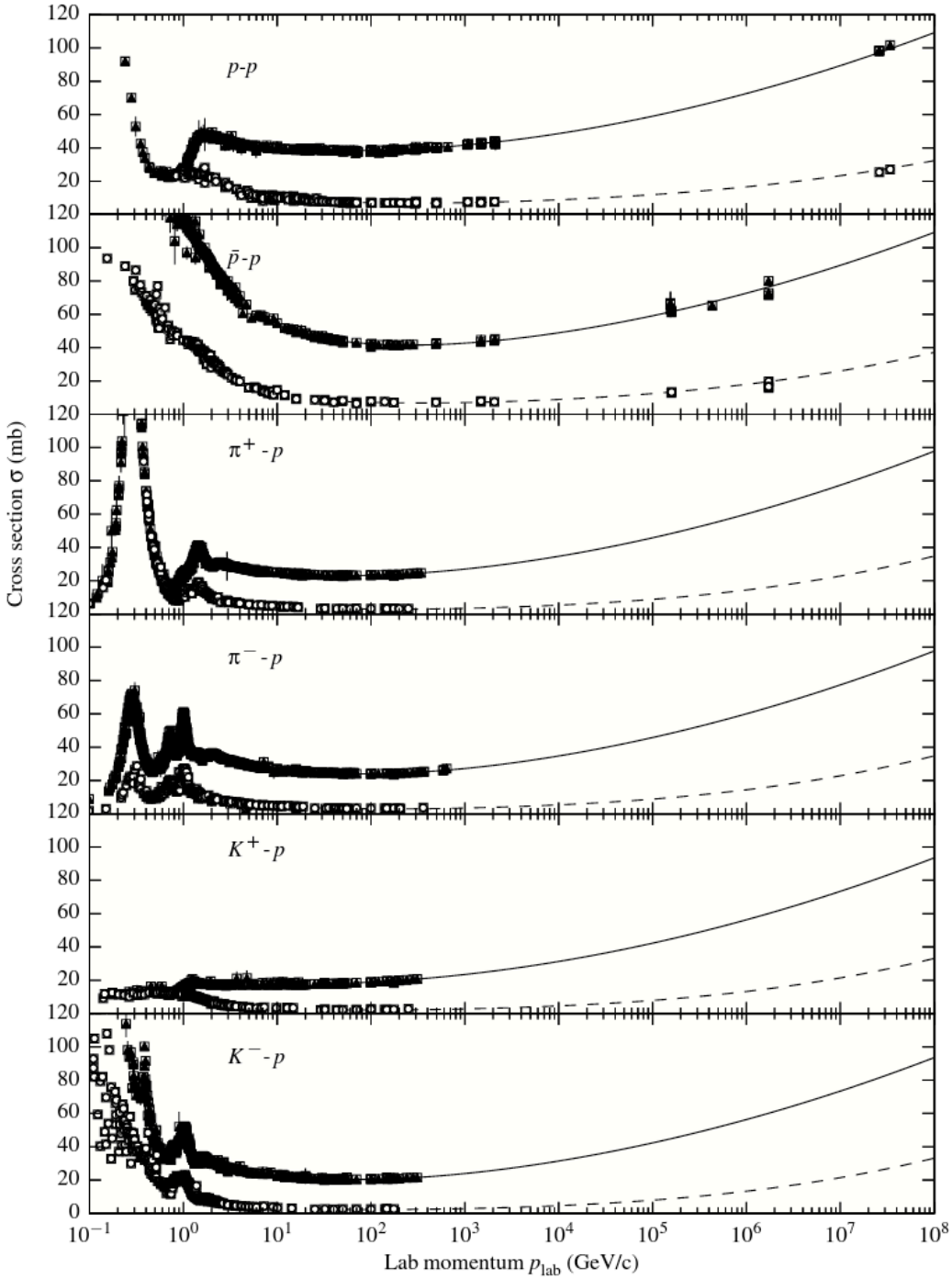

Figure 4.6 Overview of total (solid symbols) and elastic (open symbols) cross sections. The data are from the PDG compilation [10] and the curves show the 2014 fit of the PDG with a universal $\ln^2 s$ increase at high energy; see also [124].

above ~10 GeV only weak (logarithmic) dependence on energy

4.2.1 Elastic scattering and optical interpretation

Accounting for the rotational symmetry around the beam direction[2] the momentum transfer in elastic scattering, $q = p'_a - p_a$, can be expressed by the Lorentz-invariant Mandelstam variable t

$$t = q^2 = -4k^2 \sin^2 \frac{\theta^\star}{2}, \tag{4.16}$$

where $k = |\vec{p}^\star|$ is the particle momentum and $\theta^\star$ the scattering angle, both measured in the CMS.

Examples of elastic cross sections measured as function of t are shown in Figure 4.7. At small $|t|$, where the main part of the cross section is located, the t-dependence can be approximated by

$$\frac{\mathrm{d}\sigma_{\mathrm{ela}}}{\mathrm{d}t} = \left.\frac{\mathrm{d}\sigma_{\mathrm{ela}}}{\mathrm{d}t}\right|_{t=0} e^{-B_{\mathrm{ela}}(s)\,|t|}. \tag{4.17}$$

The slope parameter $B_{\mathrm{ela}}(s)$ increases with the CM energy. At energies accessible at colliders the rise is found to be proportional to $\ln s$. This dependence is expected to change asymptotically to $B_{\mathrm{ela}} \sim \ln^2 s$ at very high energy.

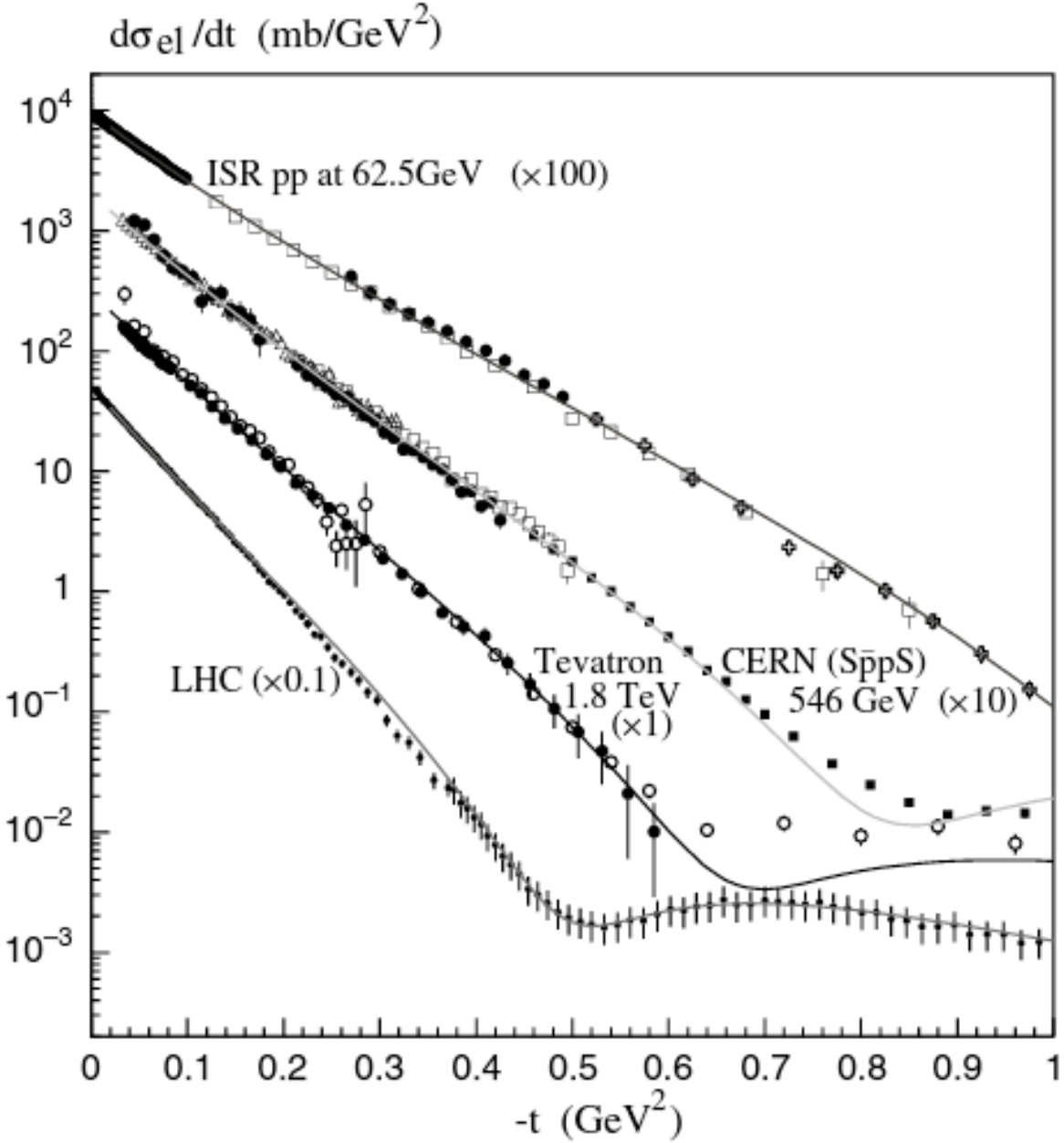

Figure 4.7 Differential cross section for elastic p-p and p-$\bar{p}$ scattering. Shown are collider data for different c.m. energies together with a model calculation. From [125], © 2014 by World Scientific, reproduced with permission.

Optical models allow a very instructive interpretation of elastic scattering data since the de Broglie wavelength λ of the interacting particles is smaller than the transverse size of the interaction region at high energy. The shape of the differential elastic cross section at small $|t|$ reflects the diffraction pattern produced by particle waves emitted from the interaction region. The observed increase of B_{ela} with energy, often referred to as *shrinkage of the diffractive cone*, corresponds to an increase of the geometric size of the interaction region. We will return to this point at the end of this Section.

Using the Lorentz-invariant scattering amplitude $A(s,t)$, the elastic cross section is given by

$$\frac{\mathrm{d}\sigma_{\mathrm{ela}}}{\mathrm{d}t} = \frac{1}{64\pi s k^2} |A(s,t)|^2 \approx \frac{1}{16\pi s^2} |A(s,t)|^2 . \tag{4.18}$$

The scattering amplitude can be expanded using the Legendre polynomials as a complete set of orthogonal functions

$$A(s,t) = 16\pi \sum_l (2l+1)\, a_l(s)\, P_l(\cos\theta), \tag{4.19}$$

with $a_l(s)$ being complex partial wave amplitudes that depend only on the interaction energy.

Each term in the sum of (4.19) corresponds to a fixed angular momentum $L = l\hbar$. Unitarity as a fundamental property of any scattering process (i.e. the sum over the probabilities of all possible final states has to be unity) leads to the *optical theorem* that provides a relation between the elastic scattering amplitude in forward direction and the total cross section (see Appendix A.4.2 for a derivation)

$$\sigma_{\text{tot}} = \frac{1}{2k\sqrt{s}} \Im m \left(A(s, t \to 0) \right) \approx \frac{1}{s} \Im m \left(A(s, t \to 0) \right). \tag{4.20}$$

Applying the optical theorem, the bound $\Im m\, a_l(s) < 1$ (see Eq. A.26) implies that the contribution of individual partial waves to the total cross section is

$$\sigma_l^{\text{tot}}(s) \leqslant \frac{4\pi}{k^2} (2l + 1). \tag{4.21}$$

This means that the number of contributing partial waves has to increase with energy to allow for the observed rise of hadronic cross sections. For example, using this bound for estimating the total cross section

$$\sigma_{\text{tot}} \sim 50\,\text{mb} \leqslant \frac{4\pi}{k^2} \sum_{l=0}^{l_{\text{max}}} (2l + 1) = \frac{4\pi}{k^2} (l_{\text{max}} + 1)^2 \tag{4.22}$$

leads to $l_{\text{max}} \sim 320$ already at $k = 100\,\text{GeV}$ and $l_{\text{max}} \sim 30,000$ at LHC energies.

4.2.2 Regge phenomenology of cross sections

Regge theory provides a framework for carrying out the summation over the partial wave amplitudes in (4.19). Combining the general assumptions of unitarity and maximum analyticity of the scattering amplitude with the empirically found relation between the mass of hadrons and their spin, as parametrized by Regge trajectories, it is possible to derive a functional form for a generic scattering amplitude at high energy. The Regge amplitude for the elastic scattering of particles a and b by the exchange of particles belonging to a given Regge trajectory α_k is

$$A_k(s,t) = \left(-\frac{1 + \tau\, e^{-i\pi\,\alpha_k(t)}}{\sin(\pi\,\alpha_k(t))} \right) \beta_{a,k}(t)\,\beta_{b,k}(t) \left(\frac{s}{s_0} \right)^{\alpha_k(t)} . \tag{4.35}$$

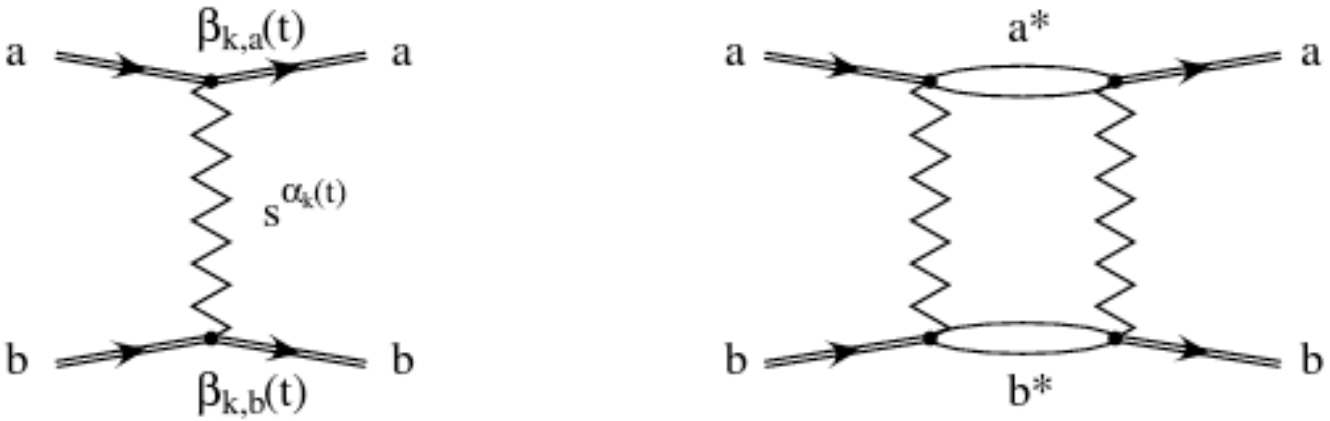

Figure 4.8 Reggeon exchange diagrams. Left: The Regge amplitude is interpreted as being built up of coupling constants and a reggeon propagator. Right: Multiple reggeon exchanges are a natural consequence if the amplitude is considered as building block of an effective field theory [127]. Excited states of the scattering hadrons, such as high-mass resonances, can be produced as intermediate states.

The contributions of all exchanged particles of a Regge trajectory are equivalent to the exchange of a quasi-particle of non-integer spin, called *reggeon*. With this interpretation the energy-independent functions $\beta_{a,k}(t)$ and $\beta_{b,k}(t)$ can be interpreted as coupling constants of the reggeon k to the incoming particles a and b; see Figure 4.8. The possible Regge trajectories to consider follow from isospin and flavor conservation at the hadron-reggeon vertices. By including Regge trajectories that do not correspond to vacuum quantum numbers, such as the exchange of charged pions or baryons, Eq. 4.35 can be applied to general $a\,b \to c\,d$ scattering processes.

The differential elastic cross section can be written as

$$\frac{\mathrm{d}\sigma_{\mathrm{ela}}}{\mathrm{d}t} = \frac{1}{16\pi}\left|\sum_k \left(-\frac{1+\tau\, e^{-i\pi\,\alpha_k(t)}}{\sin(\pi\,\alpha_k(t))}\right)\,\beta_{a,k}(t)\,\beta_{b,k}(t)\,\left(\frac{s}{s_0}\right)^{\alpha_k(t)-1}\right|^2 . \quad (4.36)$$

In most cases it is sufficient to consider only one Regge trajectory if one is interested in the small-$|t|$ region. The observed shrinkage of the diffraction peak, i.e. the energy dependence of the slope parameter B_{ela} in (4.17) is naturally understood within Regge theory. With the approximation $\beta_i(t) \sim e^{B_i t}$ for the couplings we obtain

$$B_{\mathrm{ela}} = 2B_a + 2B_b + 2\alpha'_k(0)\ln(s), \quad (4.37)$$

where we have used (3.15) for the representation of the Regge trajectory. The energy dependence of B_{ela} is thus directly linked to the slope $\alpha'(0)_k$ of the leading Regge trajectory and thus to the spin-mass relation of the exchanged particles, with B_{ela} increasing in proportion to $\ln s$. These predictions are in good agreement with measurements at not too high an energy ($\sqrt{s} \lesssim 40\,\mathrm{GeV}$).

The energy dependence of the total cross section at high energy is determined by the largest Regge intercept $\alpha_k(0)$

$$\sigma_{\text{tot}} \approx \frac{1}{s} \lim_{t \to 0} \Im m \sum_k A_k(s,t) \propto \beta_{a,k}(0)\, \beta_{b,k}(0)\, s^{\alpha_k(0)-1}. \tag{4.38}$$

All known Regge trajectories have intercepts well below unity. When a flattening of the energy dependence of the hadronic cross sections became apparent in the 1960s, Pomeranchuk postulated the existence of another Regge trajectory with intercept $\alpha(0) \approx 1$. The corresponding quasi-particle is referred to as *pomeron* and has vacuum quantum numbers, which means it couples to all hadrons in a similar way. It is assumed that glueballs are the bound states of the pomeron trajectory but experimental searches for glueballs have been inconclusive until now. The parameters of the pomeron trajectory are estimated from cross section data at high energy

$$\alpha_P(t) \approx \alpha_P(0) + \alpha'_P(t)\, t \approx 1.08 + 0.25\text{GeV}^{-2}\, t. \tag{4.39}$$

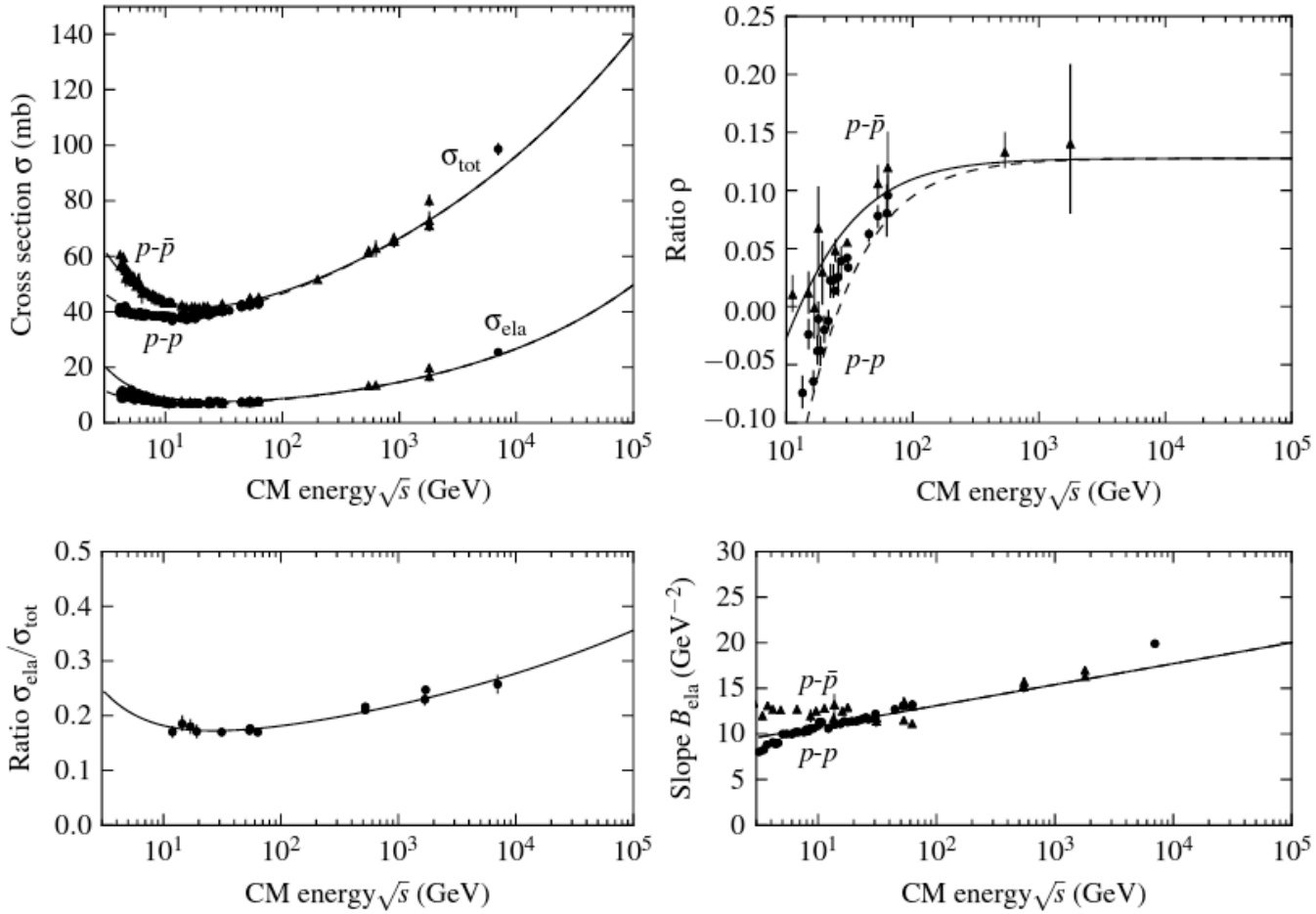

Figure 4.9 Elastic and total cross section data for p-p and p-$\bar{p}$ scattering at high energy. The curves show the Regge-inspired fit to the total cross sections by Donnachie and Landshoff [129] using the parameters derived in 1992. To calculate in addition elastic cross sections, a parametrization $\propto \ln s$ for the elastic slope has been used; see lower right panel. The data are from the compilation of the Particle Data Group [10].

The data have been fitted to the parametrization

$$\sigma_{\text{tot}} = Xs^{\epsilon} + Ys^{-\eta}, \tag{4.41}$$

with universal exponents $\epsilon = 0.0808$ (pomeron) and $\eta = 0.4525$ (reggeon) and particle-dependent constants X and Y.

Phenomenology of particle production

As indicated already by the energy dependence of the total and elastic cross sections, different particle production mechanisms are of importance at low, intermediate and high interaction energies. Interactions at very low energy, in the range from just above the particle production threshold to about $\sqrt{s} \sim 1 - 2\,\text{GeV}$, are dominated by the formation and subsequent decay of hadronic resonances. At higher energies, up to $\sqrt{s} \sim 100\,\text{GeV}$, follows a region of scaling, which is best described using hadronic degrees of freedom as done within Regge theory. At energies higher than $\sqrt{s} \sim 100\,\text{GeV}$, hadronic interactions are most efficiently described in terms of partons and their interactions. In particular, the production of partonic jets of a few GeV transverse momentum (so-called minijets) becomes a dominating phenomenon at very high energies.

4.3.1 Resonance region

Just above the energy threshold for particle production, the cross sections and distributions of secondary particles can be described by isobar models [136]. In these models, conservation of isospin[4] and angular momentum are the basic building blocks. The partial wave amplitudes of all Born diagrams of single particle exchanges or fusion to a single particle/resonance, including possible resonance excitations of the outgoing hadrons, are added up with weights and relative phases determined by symmetry relations and comparisons to measurements.

Two examples of an isobaric process included in these models are shown in Figure 4.11. Positive pions interacting with protons form a $\Delta^{++}(1232)$ resonance that subsequently decays into a π^+ and p. The contribution of the $\Delta^{++}(1232)$ resonance dominates the π^+-p cross section at low energy; see Figure 4.6. The situation is similar in the case of photon absorption shown in Figure 4.11 (right) except for the different decay channels.

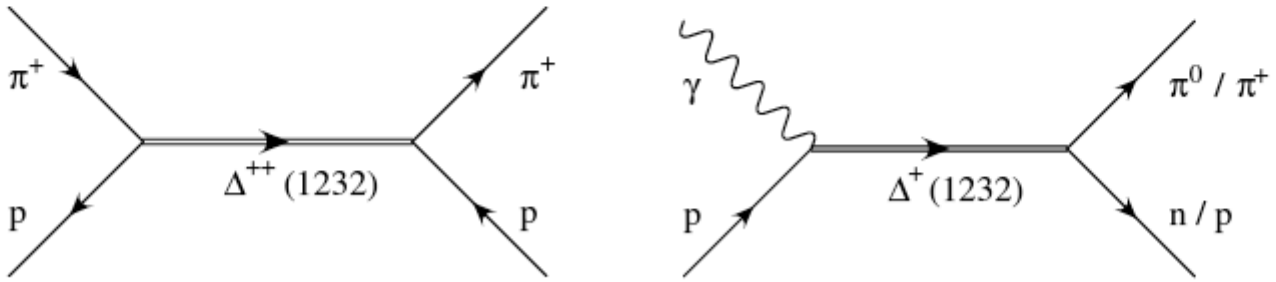

Figure 4.11 Production of the $\Delta(1232)$ resonance in the interaction of pions (left) and photons (right) with protons. While $\Delta^{++}(1232)$ decays only to π^+ p, the $\Delta^+(1232)$ decay products are π^0 p and π^+ n with the branching ratio 2 : 1.

The $\Delta^{++}(1232)$ as intermediate state has spin $J = 3/2$. The angular distribution of the decay products, which are again a π^+ and p, can be calculated with the Clebsch–Gordan coefficients [10] and is given by

$$\frac{\mathrm{d}N_\pi}{\mathrm{d}\cos\theta^\star} \propto 1 + 3\cos^2\theta^\star, \tag{4.50}$$

with $\theta^\star$ being the angle between the incoming pion (photon) and the final state pion in the c.m. system.

The spin-averaged cross section for the production of a resonance with spin J in the interaction of two hadrons with spin S_1 and S_2 is given by the Breit–Wigner cross section (see Appendix A.4.3 for a derivation)

$$\sigma_{\mathrm{BW}}(\sqrt{s}) = \frac{(2J+1)}{(2S_1+1)(2S_2+1)} \frac{\pi}{k^2} \frac{B_{\mathrm{in}}\, B_{\mathrm{out}}\, \Gamma_{\mathrm{tot}}^2}{(\sqrt{s} - m_R)^2 + \Gamma_{\mathrm{tot}}^2/4}. \tag{4.51}$$

The branching ratios of the resonance R decaying into the initial and final state particles are B_{in} and B_{out}, respectively. This non-relativistic form of the Breit–Wigner cross section is valid only for $m_R \gg \Gamma_{\mathrm{tot}}$ and energy-independent branching ratios.

4.3.2 Scaling region

The energy region of approximate scaling begins above the resonance region and extends to $\sqrt{s} \lesssim 100\,\text{GeV}$. Although the total cross sections increase by more than 10% over this energy range, the impact parameter amplitude exhibits geometric scaling. There are a number of other empirical scaling laws that apply to this energy range, which are probably related to the geometric scaling of the amplitude.

In 1969 Feynman [140] made the hypothesis that the Lorentz-invariant cross section for the inclusive production of secondary particles satisfies the scaling law

$$E\frac{\mathrm{d}\sigma_{ab\to c}}{\mathrm{d}^3 p} = f_{ab\to c}\left(x_F = \frac{p_\parallel}{p_{\parallel,\max}}, p_\perp\right), \tag{4.53}$$

at asymptotically high energies. This relation is now called *Feynman scaling*. It is a stronger formulation of the concept of *limiting fragmentation* [141], in which one assumes that only the distribution of the leading particles, stemming from the fragmentation of the projectile hadron (or, conversely, of that of the target) approaches a universal form at high energy.

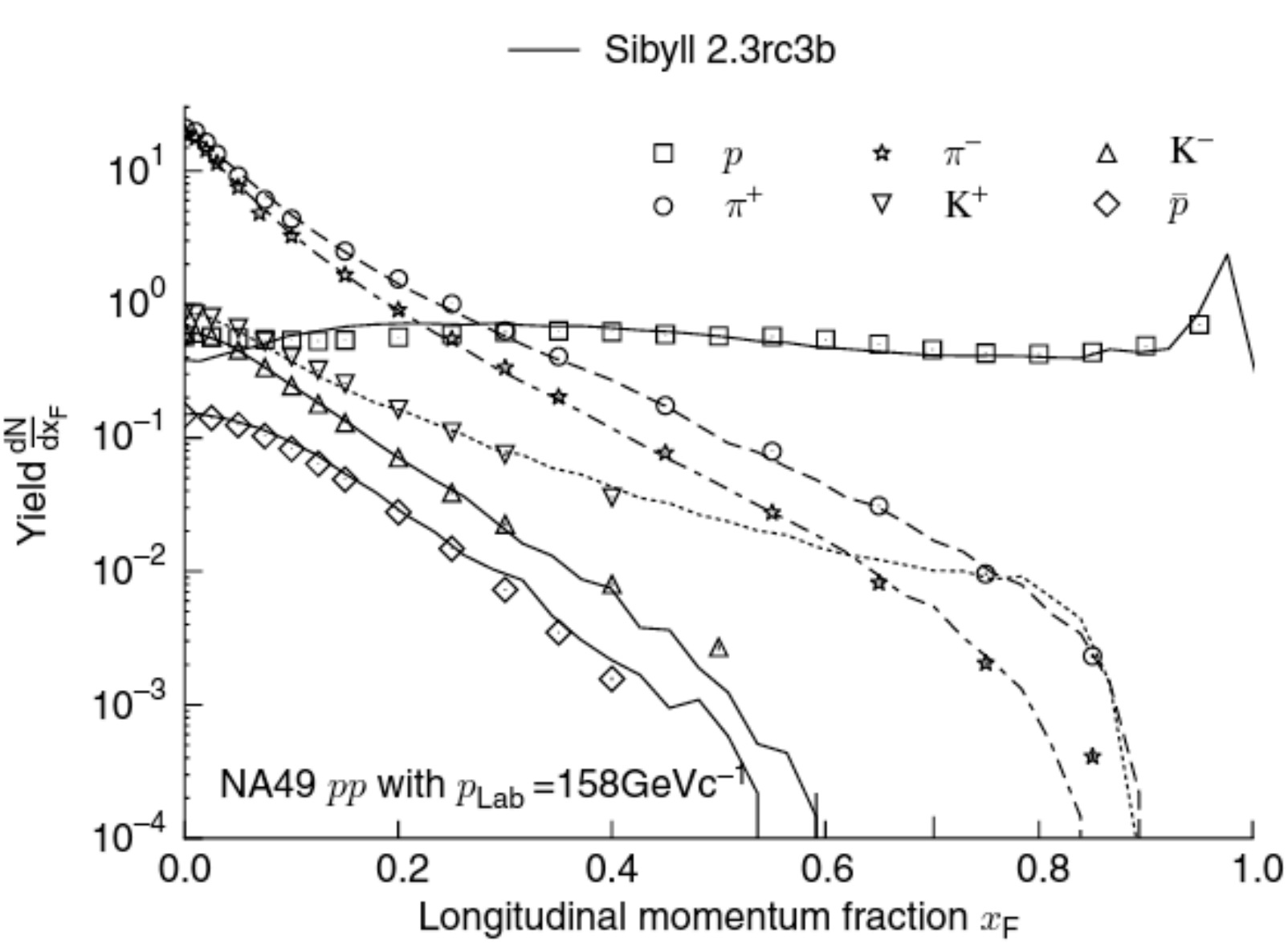

Figure 4.15 Feynman-x distributions of secondary particles in p-p interactions as measured by NA49 [152–154]. The curves show a model calculation [155]. Only the forward hemisphere is shown.

Another important phenomenological observation, and a striking difference to low-energy particle production, is the *leading particle effect*. The highest-energy secondary particle is found to carry, on average, almost 50% of the momentum of the projectile. Moreover, the leading particle has quantum numbers being either identical or, by exchange of a single valence quark, closely related to the projectile. And, as expected from our considerations in Section 4.1.3, the transverse momenta of the particles are small and follow an exponential distribution in transverse mass (see Table 4.1)

$$\frac{1}{m_\perp}\frac{\mathrm{d}N}{\mathrm{d}m_\perp} \sim e^{-m_\perp/m_0}, \tag{4.56}$$

with a mean value of $\langle p_\perp \rangle \approx 350\,\mathrm{MeV}$ for pions, slowly rising with energy.

4.3.3 Minijet region

The emergence of particle jets in the hadronic final state at $\sqrt{s} \gtrsim 100\,\text{GeV}$ and their successful description by perturbative QCD calculations encourages us to try to describe particle production in terms of asymptotically free partons.

In the perturbative picture, sea partons in a hadron are quantum fluctuations and are as such continuously generated and re-absorbed. The lifetime of partons of momentum k and virtuality Q^2 is

$$\Delta t_{\text{fluc}} \sim 1/\Delta E_{\text{fluc}} \sim \frac{1}{\sqrt{k^2} - \sqrt{k^2 - Q^2}} \approx \frac{2k}{Q^2} \tag{4.61}$$

and exceeds the typical hadronic interaction time $\Delta t_{\text{had}} \sim 5\,\text{GeV}^{-1}$ even for perturbatively accessible virtualities $Q^2 \gtrsim 4\,\text{GeV}^2$ at high energy. For the duration of a hadronic collision process, an interacting hadron can be considered as a frozen-in configuration of independently acting partons as long as the parton virtuality is not too high.

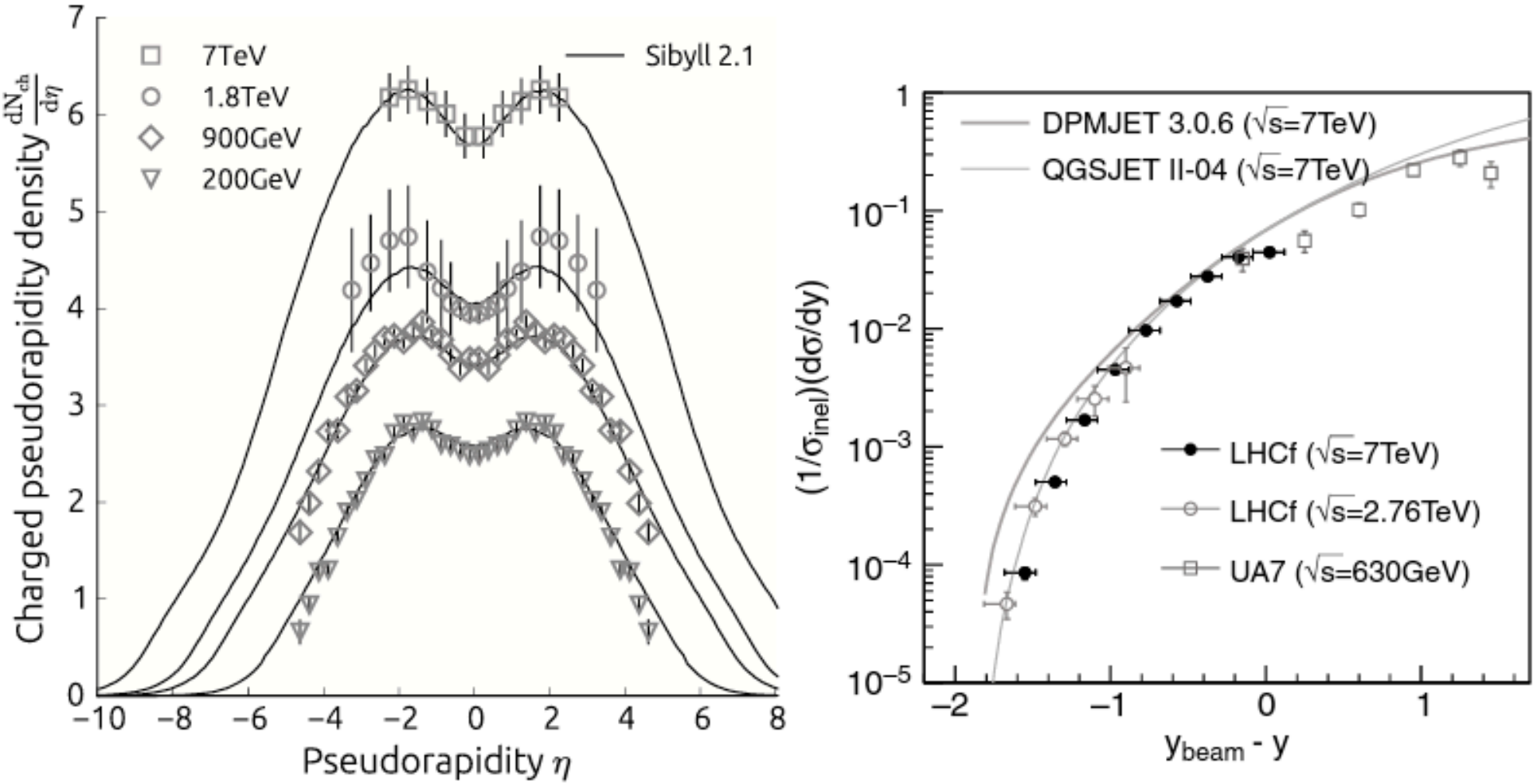

Figure 4.18 Particle production at collider energies. Left: inclusive charged particle distribution. The curves show the results calculated with the interaction model Sibyll [158] (from [165], modified). Right: neutral pion production. The measurements at different energies are shifted by the rapidity of the beam particle y_{beam} and compared with DPMJET [166] and QGSJet [162, 163] predictions (from [167]).

4.4 Nuclear targets and projectiles

It is straightforward to extend the multiple scattering formalism of Section 4.3.3 to nuclei. The transverse profiles of the projectile and target particles need to be extended to include several nucleons with positions $\vec{s}_i$ in the nucleus (see Figure 4.19). The normalization is $\int A_{\mathrm{nuc}}(b)\ \mathrm{d}^2b = A$, with A being the mass number of the nucleus. The spatial distribution of the nucleons is given by the wave function of the nucleons in the nucleus. Therefore the multiple-scattering amplitude has to be multiplied by the wave functions of the nucleon positions in the initial and final states and integrated over these positions. While this formalism provides a consistent treatment for cross sections as well as hadronic final states of hadron–hadron, hadron–nucleus, and nucleus–nucleus interactions, it does not account for possible correlations between nucleons and is not really applicable at very low energy, where the Fermi momentum of the nucleons cannot be neglected.

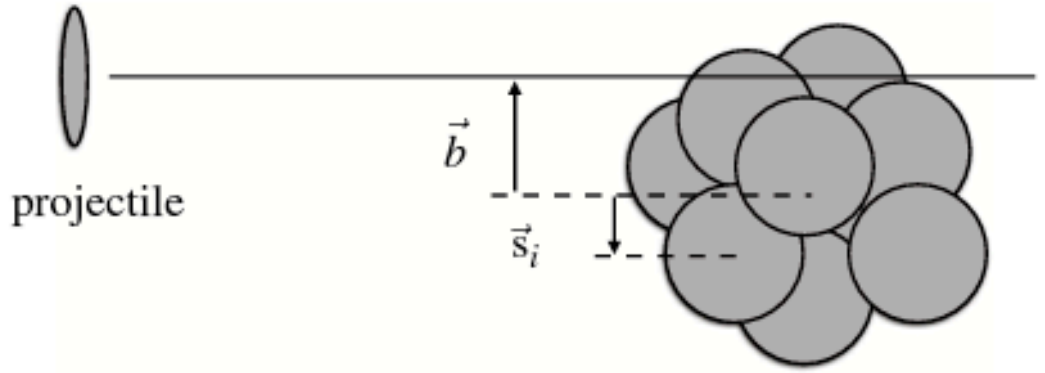

Figure 4.19 Importance of the impact parameter and the distribution of the nucleons in the target nucleus in hadron–nucleus scattering. The number of participating target nucleons is mainly determined by the geometric path of the projectile through the target.

4.4.1 Nuclear cross sections

There are three important cross sections to distinguish: the total and elastic cross sections and the cross section for *quasi-elastic* scattering. The latter appears only for nuclei and describes scattering processes in which a nucleus disintegrates, but no new secondary hadrons such as pions or kaons are produced. This can happen if, for example, two nucleons of the colliding nuclei interact elastically and, due to the recoil, one or both of the nuclei break apart.

There is some confusion in literature on how to refer to the different cross sections. Here we explicitly distinguish between the inelastic cross section given by $\sigma_{\text{ine}} = \sigma_{\text{tot}} - \sigma_{\text{ela}}$ and the *production* cross section[6]

$$\sigma_{\text{prod}} = \sigma_{\text{tot}} - \sigma_{\text{ela}} - \sigma_{\text{qela}} = \sigma_{\text{ine}} - \sigma_{\text{qela}}, \tag{4.82}$$

which describes all processes in which at least one new secondary hadron is produced, independent of the status of the nuclei after the interactions [170].

Inelastic proton–nucleus cross sections are needed for the calculation of absorption of nuclei in the interaction with hydrogen of the ISM in cosmic ray propagation. On the other hand, it is the proton–air production cross section that is relevant to air shower development because quasi-elastic interactions do not contribute to the shower evolution.

Results of a cross section calculation using the Glauber model for proton-carbon cross sections are shown in Figure 4.20 (left). The parameters used for this calculation are given in Appendix A.6. The expected cross sections slightly overestimate the measurements at high energy. This deviation is understood in terms of missing inelastic screening corrections. The curves shown in Figure 4.20 (right) are the result of a calculation with inelastic screening corrections following the parametrization of [172]. The inelastic screening contribution can be modeled by accounting for cross section fluctuations [173] or inelastic intermediate states [174]. The production cross section of p-air interactions is shown together with cosmic ray data in Figure 16.4.

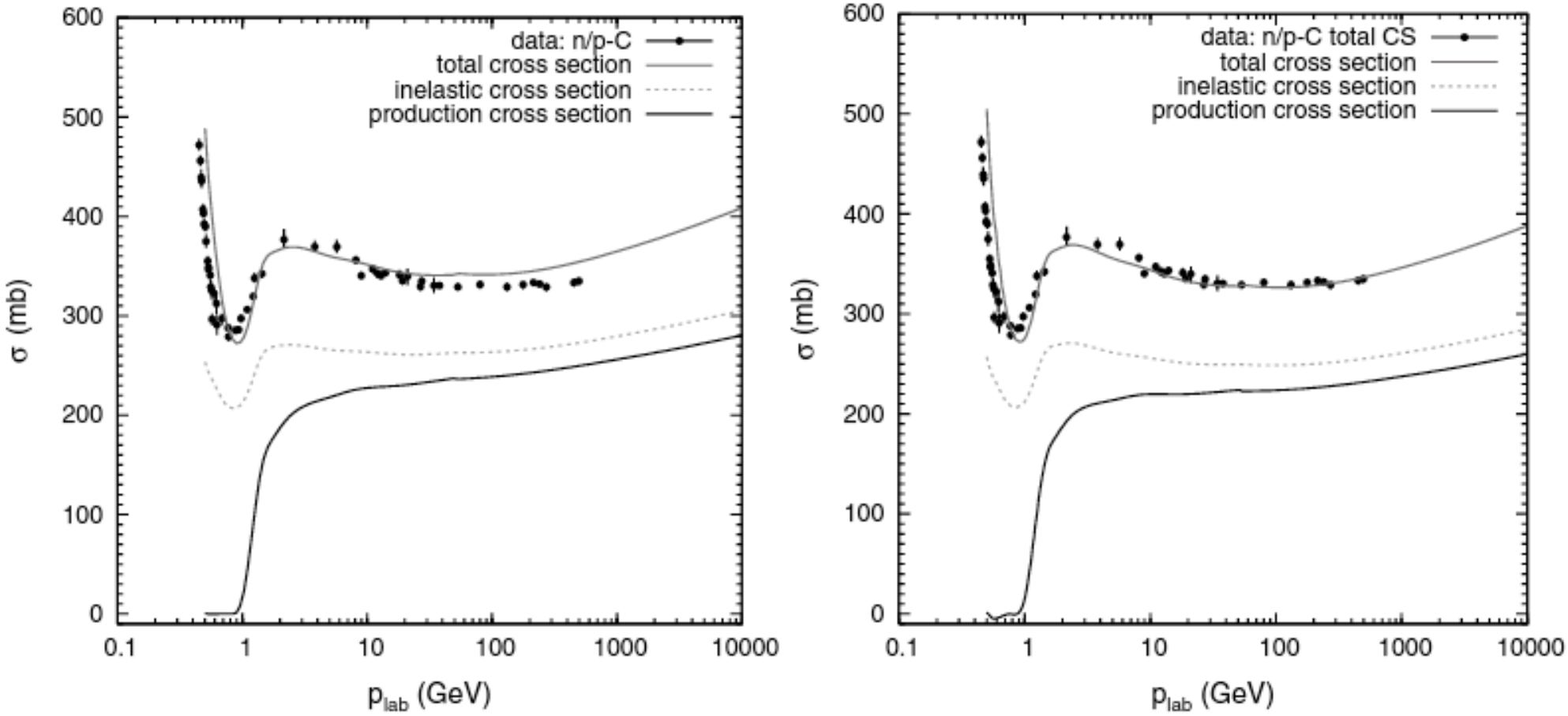

Figure 4.20 Comparison of predictions of the Glauber model of multiple scattering with data. Shown are neutron- and proton-carbon data on the total cross sections (see [171] and references therein) together with model calculations. Left: standard Glauber calculation. Right: results with inelastic screening corrections [172]. The deviations at the particle production threshold are related to the Fermi motion of nucleons, which is not accounted for in the model calculations.

Considering hadron–nucleus interactions, an approximate and much simpler version of the full Glauber theory is represented by the formula

$$\sigma_{\text{ine}}^{hA} = \int \mathrm{d}^2 b \{1 - \exp[-\sigma_{\text{tot}}^{hp} T(b)]\}, \tag{4.83}$$

which is the extension of (4.72) to nuclear targets. Here σ_{ine}^{hA} is the inelastic cross section for hadron–nucleus scattering and σ_{tot}^{hp} is the corresponding total hadron–nucleon cross section. The function $T(b)$ is the number density of target nucleons of the nucleus at impact parameter b, folded with the impact parameter profile of the amplitude for hadron–nucleon scattering (see Eq. 4.67)

$$T(b) = \int \rho_N(\vec{r})\, A_{hp}(\vec{b} - \vec{b}_N)\, \mathrm{d}z\, \mathrm{d}^2 b_N, \tag{4.84}$$

where ρ_N is the number density of nucleons at distance $r = \sqrt{b_N^2 + z^2}$ from the center of the nucleus. The production cross section $\sigma_{\text{prod}}^{hA}$ is given by an expression very similar to (4.83) [175]

$$\sigma_{\text{prod}}^{hA} = \int \mathrm{d}^2 b \{1 - \exp[-\sigma_{\text{ine}}^{hp}\, T(b)]\}. \tag{4.85}$$

Two limits follow directly from (4.85). If $\sigma_{\text{ine}}^{hp}\, T(b)$ is very small then there is no "shadowing", and

$$\sigma_{\text{prod}}^{hA} \approx \int \sigma_{\text{ine}}^{hp}\, T(b)\, \mathrm{d}^2 b \;=\; A\, \sigma_{\text{ine}}^{hp}. \tag{4.86}$$

In the opposite limit of complete screening ($\sigma_{\text{ine}}^{hp}\, T(b)$ very large) the integrand of (4.85) is approximately unity out to an effective nuclear radius R_A, so

$$\sigma_{\text{prod}} \approx \pi R_A^2 \propto A^{2/3}. \tag{4.87}$$

In the range of beam momentum $20 - 50\,\text{GeV/c}$, the A-dependence of σ_{ine}^{pA} for $A > 1$ can be approximated by (see [176])

In the range of beam momentum $20 - 50\,\mathrm{GeV/c}$, the A-dependence of $\sigma_{\mathrm{ine}}^{pA}$ for $A > 1$ can be approximated by (see [176])

$$\sigma_{\mathrm{ine}}^{pA} \cong 45\ \mathrm{mb}\, A^{0.691}. \tag{4.88}$$

This A dependence is closer to the black disk limit of (4.87) in which $\sigma^{hA} \propto A^{2/3}$, than to the transparent limit (4.86) in which the nuclear cross section is proportional to the nuclear mass number A. In contrast

$$\sigma_{\mathrm{ine}}^{\pi A} \cong 28\ \mathrm{mb}\, A^{0.75}. \tag{4.89}$$

The larger exponent in Eq. 4.89 is a consequence of the fact that $\sigma_{\mathrm{tot}}^{\pi p} < \sigma_{\mathrm{tot}}^{pp}$, so that π-nucleus scattering is farther from the black disk limit. Thus

$$\sigma_{\mathrm{ine}}^{\pi A}/\sigma_{\mathrm{ine}}^{pA} > \sigma_{\mathrm{tot}}^{\pi p}/\sigma_{\mathrm{tot}}^{pp}.$$

For the same reason $\sigma_{\mathrm{ine}}^{pA}$ increases more slowly with energy than $\sigma_{\mathrm{tot}}^{pp}$. We will also sometimes need values for inelastic cross sections between two nuclei. A standard parametrization, used originally to describe emulsion data at tens of GeV, is

$$\sigma_{A_1 A_2} = \pi R_0^2 (A_1^{1/3} + A_2^{1/3} - \delta)^2, \tag{4.90}$$

with $\delta = 1.12$ and $R_0 = 1.47$ fm [177].

4.5 Hadronic interaction of photons

The interaction of photons with hadrons and nuclei at energies close to the particle production threshold is a key process in many astrophysical environments, in which accelerated hadrons propagate in a background field of photons of the cosmic microwave background (CMB) or local sources.

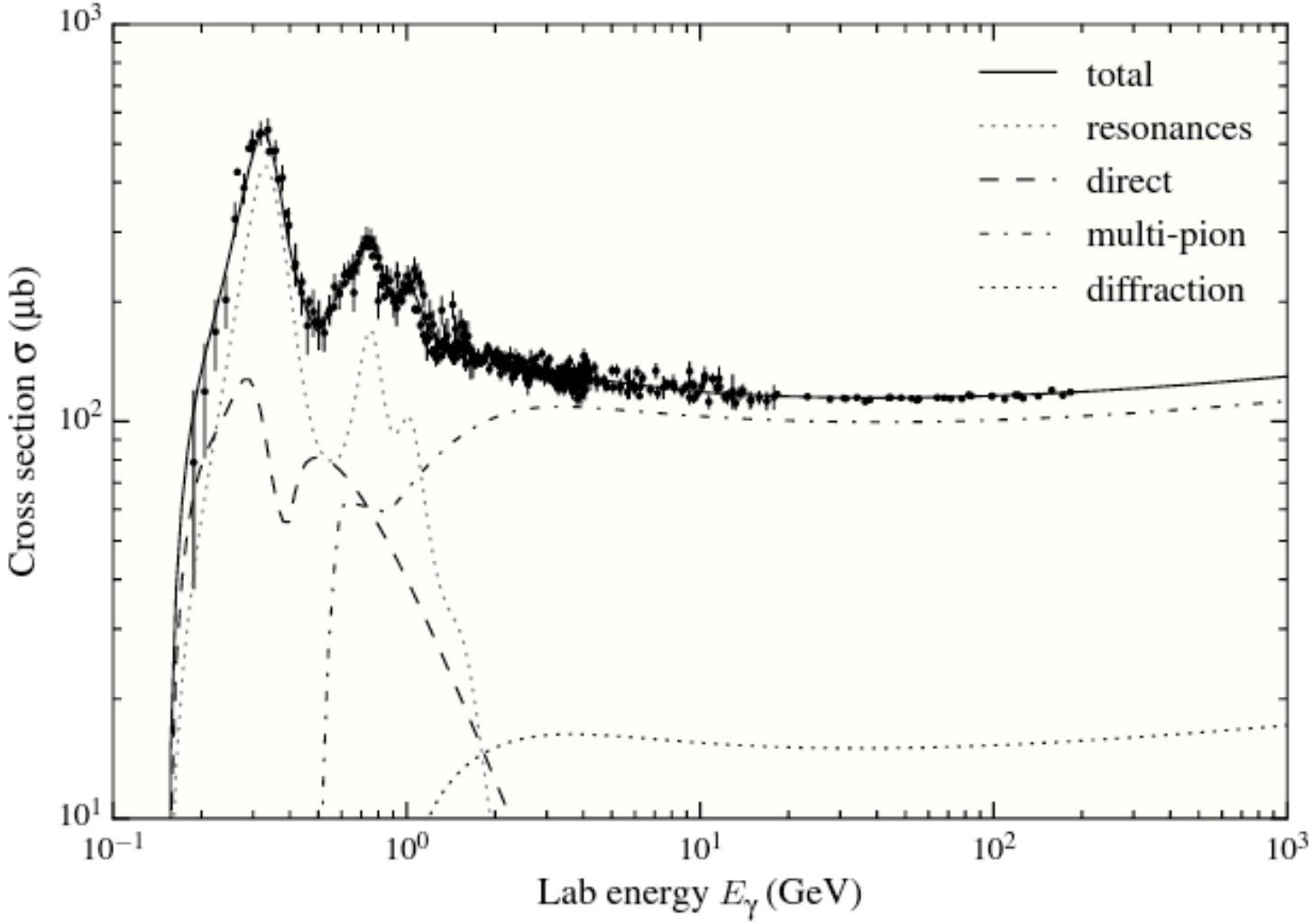

Figure 4.22 Total γ-p cross section as function of the photon energy E_γ in the lab system with the proton at rest. Four different components contributing to the hadronic cross section of photons are shown, the direct component (the photon produces directly a pion, Primakoff effect), resonance production (sum of eight individual resonances), and multipion and diffractive interactions (inelastic and elastic scattering of vector mesons) [138]. The cross section data are taken from the PDG compilation [10].